





Summer warming in the East Antarctic interior triggered by southern Indian Ocean warming

Received: 20 January 2025

Accepted: 7 July 2025

Published online: 22 July 2025

 Check for updates

Naoyuki Kurita ¹✉, David H. Bromwich ^{2,3}, Takao Kameda ⁴,
Hideaki Motoyama ⁵, Naohiko Hirasawa ⁵, David E. Mikolajczyk ⁶,
Linda M. Keller ^{6,7} & Matthew A. Lazzara ^{6,8}

The effects of global warming on Antarctica's interior, which is covered by a huge ice sheet, remain uncertain. A major reason for this is the lack of long-term observations of near-surface temperatures in the interior region, compounded by significant gaps in the available dataset. Here, we present a complete temperature record from three inland stations (Mizuho, Relay Station, and Dome Fuji), where gaps have been filled with corrected reanalysis data. At all stations, the record revealed a statistically significant warming in annual mean temperature from 1993 to 2022, with the most rapid warming occurring during the half-year mean from October to March. At the same time, a rapid warming of sea surface temperature (SST) in the southern Indian Ocean strengthened the SST fronts over the Subtropical Frontal Zone (STFZ), resulting in a meridional dipole response in the atmosphere and an increased advection of warm air into the interior of the East Antarctic Ice Sheet (EAIS). Over the past 30 years, the SST gradient in the STFZ has increased by around 20%, making the occurrence of the meridional dipole pattern more likely. Consequently, the climate of Antarctica's interior is susceptible to the impact of climate change in the southern Indian Ocean.

The world is experiencing rising temperatures in response to human-induced global warming. However, there are few reports on the impact of anthropogenic warming on the East Antarctic Ice Sheet (EAIS), which contains the vast majority of the world's glacial ice. The surface air temperature (SAT) variability on the EAIS is closely related to the phase of the Southern Annular Mode (SAM)¹. A positive phase of the SAM is characterized by strengthened westerlies over the Southern Ocean, which reduce meridional advection of warm air into the continent, resulting in cooler temperatures over East Antarctica^{2–6}. The trend of SAM towards its positive phase in recent decades has led to a

cooling effect. Therefore, modest temperature changes or cooling trends during the second half of the 20th century are explained by SAM-induced cooling masking anthropogenic warming in East Antarctica^{2–4,7}. For this reason, the EAIS is considered less sensitive to anthropogenic warming than other Antarctic regions⁸.

However, despite the continued positive SAM trend, albeit with a slight weakening in the early 21st century, a widespread warming in the EAIS has been observed in the 21st century^{4,7,9–12}. The atmospheric circulation pattern associated with the positive SAM phase has changed to a more asymmetric pattern^{9,11,13–15}. This circulation change may

¹Institute of Space-Earth Environmental Science(ISEE), Nagoya University, Nagoya, Aichi, Japan. ²Polar Meteorology Group, Byrd Polar and Climate Research Center, The Ohio State University, Columbus, OH, USA. ³Atmospheric Sciences Program, Department of Geography, The Ohio State University, Columbus, OH, USA. ⁴Snow and Ice Research Laboratory, Kitami Institute of Technology, Kitami, Hokkaido, Japan. ⁵National Institute of Polar Research (NIPR), Tachikawa, Tokyo, Japan. ⁶Antarctic Meteorological Research and Data Center, Space Science and Engineering Center, University of Wisconsin-Madison, Madison, WI, USA. ⁷Department of Atmospheric and Oceanic Science, University of Wisconsin-Madison, Madison, WI, USA. ⁸Department of Physical Sciences, School of Science, Technology, Engineering, and Mathematics, Madison Area Technical College, Madison, WI, USA. ✉e-mail: nkurita@nagoya-u.jp

have attenuated the SAM-induced cooling and made the EAIS more susceptible to anthropogenic warming than previously thought. Alternatively, warming in the EAIS may be attributed to the climate change that triggered the SAM pattern change, but the mechanism of the warming is unclear.

Assessing the climate change across the EAIS remains a major challenge due to the insufficient coverage of observing networks¹. The majority of the staffed stations are situated along the coast, with only two stations (Amundsen-Scott and Vostok) with long-term temperature records located in the interior of the continent¹⁶. Despite the sparsity of observing stations in the EAIS, the observed SAT records since 1999 indicate widespread warming trends during the austral spring (September to November) and summer (December to February), particularly in the Indian Ocean sector^{7,9,12}. This is consistent with the land surface temperature trend over Antarctica, as obtained from satellite observations¹⁷. The satellite-derived surface temperature trend map from 2000 to 2018 illustrates the most pronounced warming over the interior of the Indian Ocean sector of East Antarctica in the austral spring and summer. Similarly, most reanalysis datasets also exhibit a robust warming trend in the interior region, although the spatial pattern of the SAT trend differs among the different reanalysis data^{12,18}. These suggest that the warming in the inland regions may be occurring at a faster rate than in coastal areas. Nevertheless, there are no reliable observations that can be used to assess the climate change in this region.

Here, we present a novel SAT record for the past three decades with the objective of determining the SAT trend over the interior of the EAIS and understanding the mechanisms involved. The monthly-means of the 30-year long time series were constructed from the integration of multiple automatic weather station (AWS) records in the eastern Dronning Maud Land (DML) from 1993 to 2022¹⁹ and are utilized in this study. The observations represent historical records from three AWS in the DML: Mizuho(MIZ), Relay Station(RLS), and Dome Fuji (FUJ) (Fig. 1). Nevertheless, there are several concerns that need to be addressed in order to employ the AWS observations in the investigation of climate variability and change in Antarctica. The concerns include a warm-temperature bias in summer due to intense solar radiation and insufficient ventilation of the temperature sensor within its radiation shield, non-adjustment of the height changes of the temperature sensor due to snow accumulation, and systematic errors due to changes to the equipment at the station during the long-term observations. In this study, these issues were quantified by comparing them to reliable temperature measurements and subsequently eliminating them¹⁹. Then, a rigorous quality control of the data was conducted in accordance with the protocol established by the Scientific Committee on Antarctic Research (SCAR) Reference Antarctic Data for Environmental Research (READER) database¹⁶. These careful considerations allow us to use AWS observations to study climate change. More details on the quality controls of AWS data are described in our previous study¹⁹ and Methods.

Missing observations have been filled in with bias-corrected temperature data from the ERA5 reanalysis²⁰. ERA5 is less influenced by the assimilation of AWS data and is capable of reasonably predicting the near-surface temperature at these three AWS, despite a slight warm bias (see Methods and Supplementary Methods). In this study, the warm biases of ERA5 are quantified by comparison with observations and then removed using a linear regression model. The uncertainty of the monthly bias-corrected ERA5 data is less than 1.4 °C (Supplementary Fig. S11). This is nearly equivalent to, or less than, the measurement error of AWS temperature observation. Furthermore, it is much smaller than the standard deviations of monthly temperatures. These make it suitable for completing missing data. Details of the reason for selecting ERA5, the techniques used to correct the temperature bias in ERA5 and to fill in the missing observations are described in Methods and Supplementary Methods.

The observed variability in the annual mean SAT at each station captures broader-scale changes due to the high correlation between the stations (Fig. 1). Furthermore, the significant correlation between the annual and seasonal mean temperatures at Relay Station, located in the middle of these three AWS, and those observed at inland stations in the EAIS and other coastal stations in the Indian Ocean sector of East Antarctica, suggests that this new record may offer insight into large-scale temperature changes (Supplementary Fig. S1).

Results

Temperature trends in the inland DML

The time series of annual mean SAT records from the stations in the eastern DML over the last 30 years, along with the trends at each station, are presented in Fig. 1c–g. The Mann-Kendall trend test is used to determine whether or not there is a statistically significant trend over the past 30-years. All inland stations experienced statistically significant ($p < 0.05$) warming trends of 0.45 ± 0.39 °C dec⁻¹ at FUJ, 0.50 ± 0.38 °C dec⁻¹ at RLS and 0.72 ± 0.34 °C dec⁻¹ at MIZ, although coastal stations have not experienced significant warming. For MIZ, however, the larger warming trend may be artificial, due to the fact that nearly half of the observations from 1993 to 2022 are missing. The warming trends observed at FUJ and RLS from 1993 to 2022 are of a comparable magnitude to those observed at the other Plateau stations during the same period (0.56 ± 0.36 °C dec⁻¹ at Amundsen-Scott and 0.53 ± 0.41 °C dec⁻¹ at Vostok). During the four years of the record-high annual mean SATs observed at Amundsen-Scott station (2002, 2009, 2013 and 2018)¹¹, maxima of SATs were also observed at FUJ and RLS (Fig. 1c, d).

Seasonally, RLS and FUJ experienced statistically significant ($p < 0.05$) warming in austral spring of 0.61 ± 0.36 °C dec⁻¹ and 0.56 ± 0.37 °C dec⁻¹ and in austral summer of 0.45 ± 0.42 °C dec⁻¹ and 0.65 ± 0.38 °C dec⁻¹, respectively. Neither station experienced statistically significant warming in austral autumn and winter. The concurrent slight warming of coastal stations on the EAIS⁷ lends further support that this observed warming extends beyond inland DML. Spring warming was observed at both stations from October, and a rapid warming is evident in the half-year mean SAT from October to March, which hereafter is referred to as the warm half-year (Fig. 1h–l). In contrast, there is no significant trend over the eastern DML during the rest of the year, from April to September, referred to hereafter as the cold half-year (Fig. 1m–q). The inter-annual variability of the cold half-year mean SAT was strongly influenced by the SAM variability (Supplementary Fig. S2).

It is noteworthy that the warming trend (statistically significant at $p < 0.05$) in the warm half-year (0.89 ± 0.30 °C dec⁻¹ for FUJ, 0.80 ± 0.34 °C dec⁻¹ for RLS) appears to be more pronounced than that in the spring and summer means and corresponds to approximately twice the annual mean trend. The robustness of the clear warming trend is confirmed by the fact that the infilling of missing observations with bias-corrected ERA5 data does not contribute to the trend (Supplementary Fig. S12). These suggest that the warmth of spring persists throughout the summer months and that the recent annual-mean warming trend observed in the interior DML is attributed to the rapid warming in the warm half-year.

Identification of key drivers of warming in the inland DML

Temperatures in the interior of Antarctica are sensitive to the north-south flow of air masses that are associated with either cyclonic or anticyclonic circulation^{11,21–25}. It is well known that the variability of sea surface temperature (SST) in the tropics influences the atmospheric circulation in the Antarctic region^{11,18,26–29}. The warming trend at Amundsen-Scott and the surrounding plateau region during the 21st century has been attributed to more cyclonic conditions in the Weddell Sea, which would enhance the warm northerly flow toward the Antarctic interior. The increased cyclonic activity has been linked to the Rossby wave teleconnection triggered by anomalous convective activity due to an increase in SST in the tropical Pacific¹¹. Interestingly,

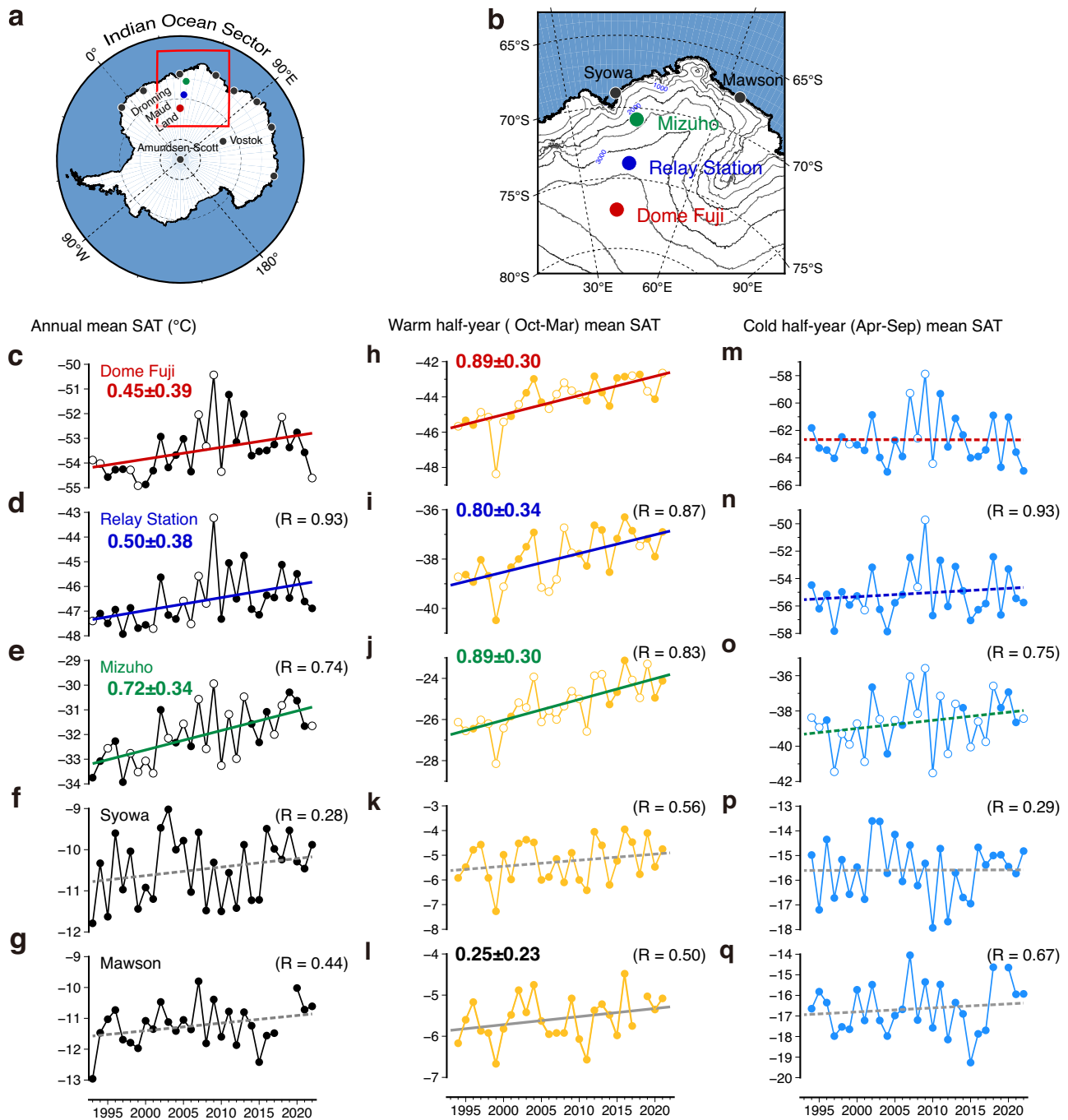


Fig. 1 | Surface air temperature (SAT) changes in the Indian Ocean sector in East Antarctica. Map of Antarctica (a) with an enlarged Indian Ocean sector in East Antarctica showing the locations of stations referred to in the text (b). c–g The time series of annual mean SAT are shown for Dome Fuji (FUJ, (c)), Relay Station (RLS, (d)), Mizuho (MIZ, (e)), Syowa (SWA, (f)), and Mawson (MAW, (g)). h–l Same as (c–g), but for warm half-year (October–March) mean. m–q Same as (c–g), but for cold half-year (April–September) mean. For time-series at FUJ, RLS, and MIZ, open circles indicate the parts of the dataset with more than one-third missing

observations, otherwise solid circles are used (see Methods and Supplementary Methods). Plots for SWA and MAW are obtained from READER database¹⁶. Solid linear lines indicate statistically significant ($p < 0.05$) linear trends, otherwise dashed lines are used. Annual and half-year mean temperature trends for 1993–2022 (1993–2021 for warm half-year), with the 95% confidence intervals, are presented at stations where a statistically significant linear trend was identified. The correlation coefficient between the FUJ and the data from each site for 1993–2022 (1993–2021 for warm half-year) is shown in parentheses.

the variability of warm half-year mean temperatures at RLS exhibits a significant correlation ($R=0.66$; $p < 0.05$) with the variability observed at Amundsen-Scott (Supplementary Fig. S1). A distinct warming trend of $0.75 \pm 0.42^\circ\text{C dec}^{-1}$ during the warm half-year has also been observed at Amundsen-Scott. These results suggest that cyclonic anomalies in the Weddell Sea, attributed to tropical Pacific climate variability, may influence temperatures at RLS in a similar way to those

at Amundsen-Scott. However, the spatial distribution correlated with RLS temperature variability shows that thermal advection from the Indian Ocean plays a dominant role on the temperatures at RLS (Supplementary Fig. S1). And given that SST changes in the tropical Pacific have little effect on RLS temperatures during the warm half-year (Supplementary Fig. S3a), the tropical forcing is not a major contributor to the warming in the DML. During the austral summer, the

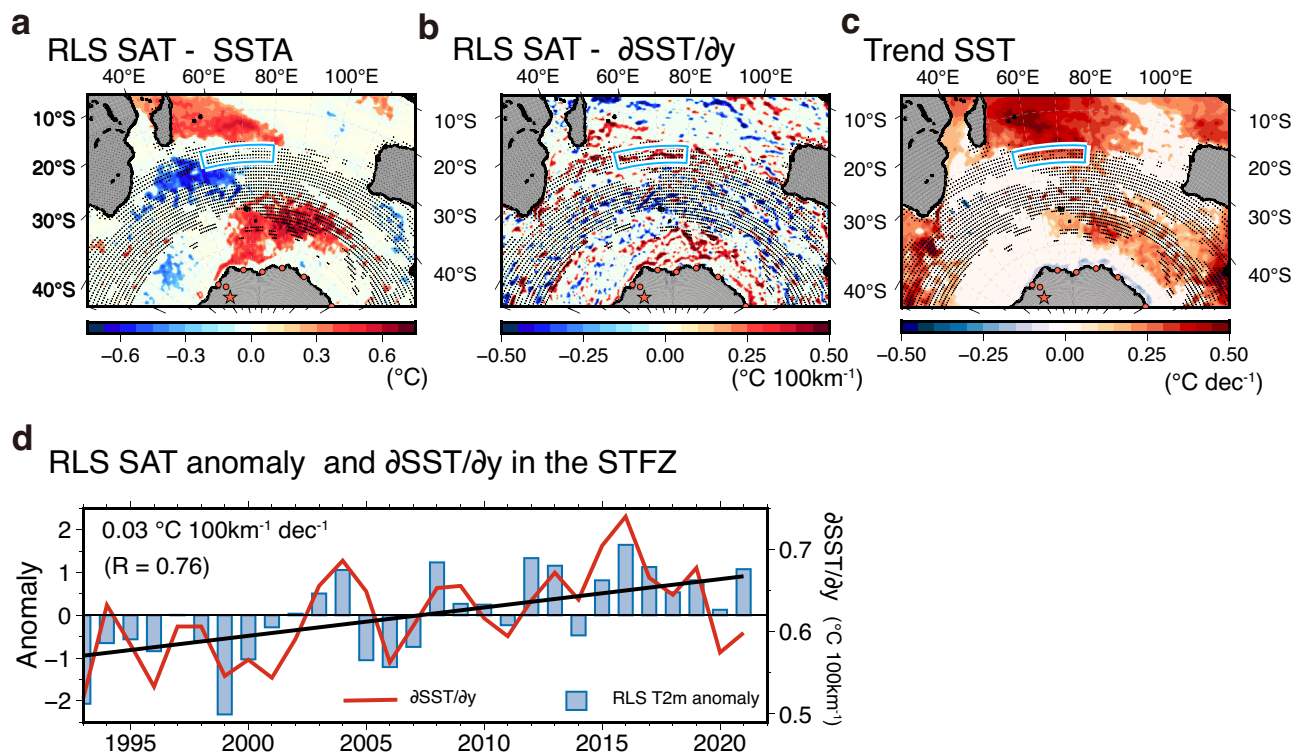


Fig. 2 | Sea surface temperature (SST) frontal variability in the southern Indian Ocean contributing to Relay Station (RLS) temperature changes over the past three decades. a, b Spatial regressions of the detrended warm half-year mean RLS surface air temperature (SAT) with SST anomaly (SSTA) (units: °C) (a) and SST meridional gradient ($\partial\text{SST}/\partial y$, units: °C 100 km⁻¹) (b) for 1993–2021. **c** The trend of warm half-year mean SST for 1993–2021. Only data points falling within the 90% confidence interval are plotted. The dots indicate the frontal zone with SST meridional gradient above 0.6 °C 100 km⁻¹. **d** The time series of the warm half-year

mean anomalies of the RLS SAT (light blue bar) and of $\partial\text{SST}/\partial y$ in the subtropical frontal zone (STFZ) (30°–35°S; 55°–80°E) (red line). The trend of $\partial\text{SST}/\partial y$ in the STFZ is shown at the upper left. The correlation of warm half-year mean RLS SAT and $\partial\text{SST}/\partial y$ in the STFZ for 1993–2021 periods is given in parentheses at the upper left. For all maps, the STFZ used for comparison with the RLS SAT is indicated by the blue box. The red star and circles are the locations of RLS and staffed stations with long-term temperature records.

tropical-polar teleconnection is reduced due to the absence of subtropical westerlies, which serve as the primary pathway for the propagation of the Rossby waves from the tropics to the high latitudes^{28,30}.

An alternative source of the recent warming in the DML is variability in the strength and position of the circumpolar westerlies^{31,32}. While the westerlies are predominantly a zonally symmetric flow, they occasionally change into an asymmetric circulation, such as the quasi-stationary zonal wavenumber 3 pattern³³. The asymmetric circulation is associated with a pattern in which northward and southward flows strengthen, and enhanced meridional heat transport between mid- and high latitudes has a strong impact on Antarctic temperatures^{11,13–15}. During the austral summer, planetary wave activity in the southern hemisphere reaches minimum amplitude, and thus the annular flow is dominant^{6,14,34}. However, an asymmetric pattern is triggered by a Rossby wave source adjacent to the westerlies in the mid-latitudes. During the austral summer, the positive SST anomalies over the subtropics lead to anomalous convection, and the vortex stretching associated with enhanced convection triggers the formation of a Rossby wave train³⁵. This suggests that SST variability in the subtropics adjacent to the westerlies influences atmospheric circulation in the Antarctic climate. The hypothesis is supported by the fact that the spatial regression pattern between SAT at RLS and the SST anomaly field (Supplementary Fig. S3, Fig. 2a) reveals the most robust signal in the southern Indian Ocean. Here we focus on the mechanism by which changes in subtropical Indian Ocean SSTs have an impact on Antarctic temperatures.

The regression map in Fig. 2a shows a distinct SST anomaly with a positive-negative-positive tripole pattern along the meridian from the

subtropics to the subantarctic over the southern Indian Ocean. It is notable that the region between the positive SST anomaly in the subtropics and the negative SST anomaly in the mid-latitudes coincides with the Subtropical Frontal Zone (STFZ), which is composed of multiple SST fronts with northwest-southeast alignment^{36,37} (Fig. 2a). Similarly, the area between the negative SST anomaly in the mid-latitudes and the positive SST anomaly in the subantarctic corresponds to the Agulhas Front and Subantarctic Front, a sharp transition zone between the southern gyre boundary and the subantarctic region³⁸. The dipole structure of subtropical SST warming and mid-latitude SST cooling indicates an increasing SST gradient, which corresponds to the strengthening of the STFZ (Fig. 2b). In contrast, the pattern of mid-latitude SST cooling and subantarctic SST warming decreases the SST gradient, so that the Agulhas Front and Subantarctic Front weaken. This suggests that an enhanced STFZ may be a key driver of the atmospheric circulation leading to Antarctic SAT variability. Indeed, the observed RLS SAT demonstrates a robust correlation ($R = 0.76$; $p < 0.05$) with the meridional SST gradients in the STFZ region (30°–35°S; 55°–80°E) from 1993 to 2021 (Fig. 2d). The SST gradients in the STFZ are strengthened as the area of accelerated warming in the southern Indian Ocean extends north of the STFZ region (Fig. 2c). The strengthening of the STFZ may play an important factor in the warming of the interior of the DLM in EAIS.

The variability of SST fronts exerts a significant influence on the atmospheric circulation through ocean-atmosphere interaction^{39–42}. The 300 hPa geopotential height anomalies (Z300), which are associated with the variability of the STFZ, demonstrate a meridional dipole pattern from the mid-latitude Indian Ocean to the interior of

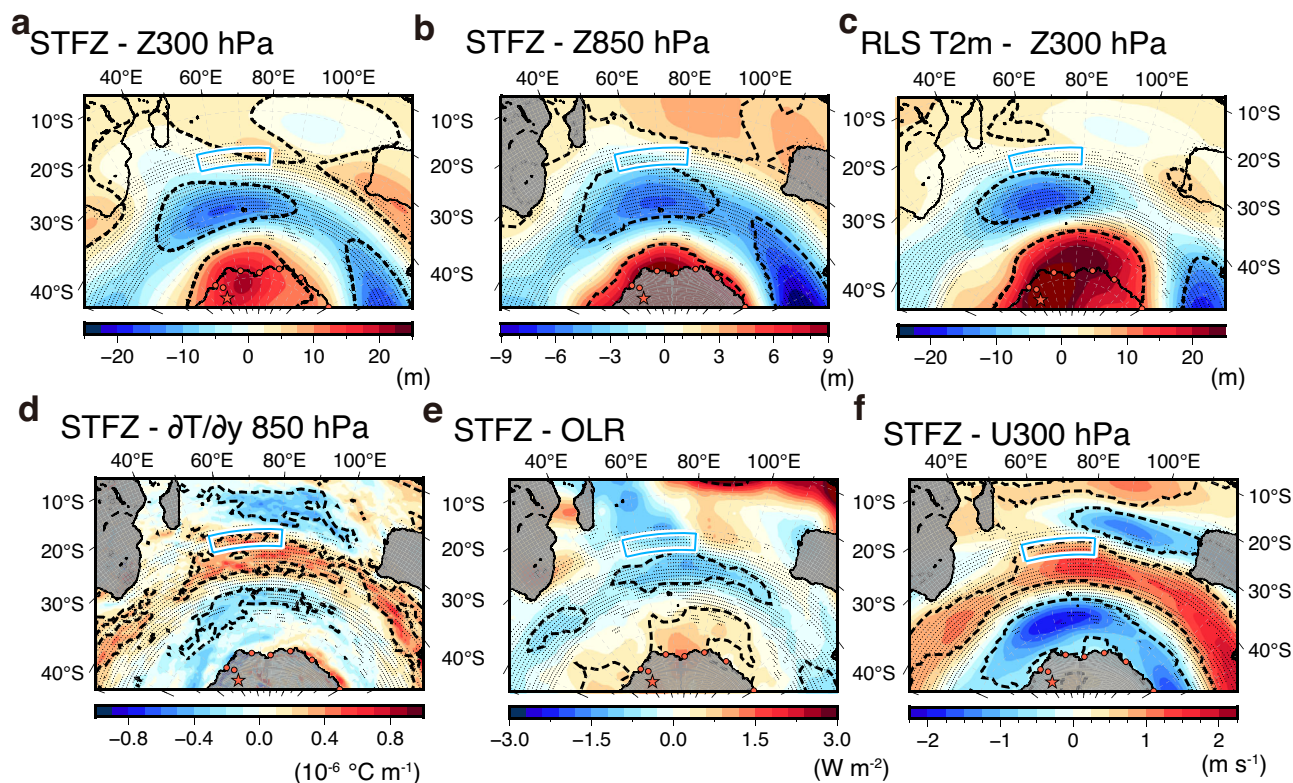


Fig. 3 | Atmospheric response to the variability of subtropical frontal zone (STFZ). **a–f** Spatial regressions of the detrended warm half-year mean $\partial SST/\partial y$ in the STFZ region with geopotential height at 300 hPa (units: m) (**a**) and at 850 hPa (units: m) (**b**), air temperature gradient at 850 hPa ($\partial T/\partial y$, units: $10^{-6} \text{ °C m}^{-1}$) (**d**), outgoing longwave radiation (OLR, units: W m^{-2}) (**e**), and zonal wind speed at 300 hPa (units: m s^{-1}) (**f**). **c** Same as (**a**), but for regressions with the detrended warm

half-year mean Relay Station (RLS) temperature. The thick black dashed lines indicate the 90% confidence level of the regression slopes. The black dots indicate the sea surface temperature (SST) frontal zone with SST meridional gradient ($\partial SST/\partial y$) above $0.6 \text{ °C } 100 \text{ km}^{-1}$. The STFZ region is indicated by the blue box. The red star and circles are the locations of RLS and staffed stations with long-term temperature records.

East Antarctica (Fig. 3a). This circulation pattern is almost identical to the Z300 anomalies, which exhibited a correlation with the RLS temperature (Fig. 3c). The positive (anticyclonic) Z300 anomaly over East Antarctica would enhance the warm northerly flow toward the interior of the EAIS. The three AWS (MIZ, RLS, FUJ) are located on the western flank of the anticyclonic anomaly, where warm northerly flow dominates. The increased occurrence of this dipole pattern associated with the strengthening of the STFZ may lead to a warming of inland DLM.

In the mid-latitudes, the negative (cyclonic) Z300 anomaly is evident above the cold SST anomalies, and its vertical structure is barotropic (Fig. 3a, b). This atmospheric structure is consistent with the response to SST anomalies in the subtropical frontal zone (Fig. 4)^{43–46}. The enhanced oceanic front leads to a strengthening of the baroclinity in the low-level atmosphere and thus to stronger synoptic-scale transient eddy activities, represented as a storm track. These transient eddies exert an influence on atmospheric circulation in the upper troposphere by transporting heat and momentum (vorticity flux). The formation of a cyclonic anomaly with barotropic structure on the polar side of the oceanic front is a common response to an increase in the transient eddy vorticity forcing^{42,43,47,48}. These explanations are consistent with the fact that negative Z300 anomalies in the mid-latitude Indian Ocean correspond to both positive low-level atmospheric baroclinity and negative outgoing longwave radiation (OLR) anomalies, i.e., an increase in cloudiness, associated with enhanced STFZ (Fig. 3d, e). In addition, enhanced 300 hPa zonal westerlies along the STFZ are also collocated with negative OLR anomalies which extend zonally downwind due to the transport of vorticity fluxes into the mean westerly flow (Fig. 3f).

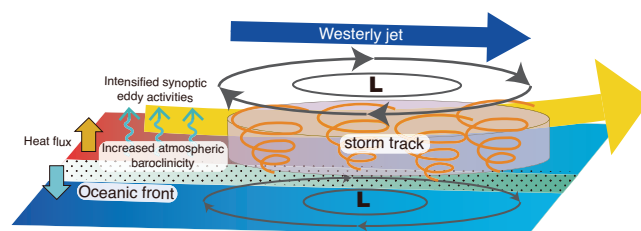


Fig. 4 | Atmospheric response to variability of sea surface temperature (SST) front. The sensible heat flux contrast across the oceanic fronts maintains the surface air temperature difference and thus increases the atmospheric baroclinity, including more active transient eddy activities that increase transient eddy vorticity forcing. The increased transient eddy vorticity forcing forms an equivalent barotropic geopotential low over the cooling SST, which is located south of the oceanic fronts. The atmospheric response to the transient eddy vorticity forcing reaches into the upper troposphere and influences the westerlies in the southern Indian Ocean.

These atmospheric responses to STFZ variability are remarkably an opposite pattern to the south of the Subantarctic Front, which anchors the westerly jet axis. The weakening of the Subantarctic Front leads to a decrease in low-level atmospheric baroclinity, which in turn reduces transient eddy activities in the westerly jet region. The weakened storm track activity (positive OLR anomalies) deposits decreased cyclonic vorticity over the south side of westerly jet axis, thereby driving anticyclonic anomalies that further weaken the westerlies in the upper atmosphere.

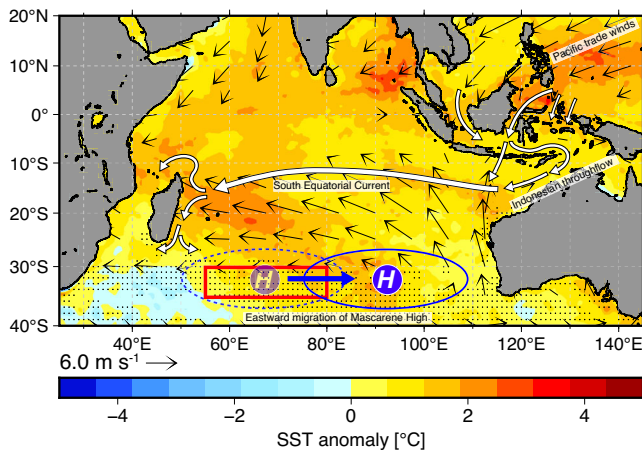


Fig. 5 | Climatological and hydrographic background of southern Indian Ocean during warm-half year. Sea surface temperature (SST) change from the first half of the observation period (1993–2007) to the second half (2008–2021), with Interdecadal Pacific Oscillation (IPO) induced warm water pathways (open white arrows) from the Pacific to the Indian Ocean. The black arrow represents the warm half-yearly mean surface wind during the observation period. The letter H with a solid (dashed) blue circle is the position of the Mascarene High after (before) the warming of the Indian Ocean. The dots indicate the frontal zone with a SST meridional gradient above $0.6\text{ }^{\circ}\text{C}\ 100\ \text{km}^{-1}$. The subtropical frontal zone (STFZ) region is indicated by the thick red box.

The feature of decreasing the pressure gradient between the mid-latitudes and Antarctica, along with a weaker and equatorward shift of the westerlies, is consistent with a negative SAM pattern that increases meridional warm air advection into the interior of Antarctica^{2,3,5,6}. The three strongly negative SAM phases (SAM index < -0.4) in the second half of the observation period (2008–2022) correspond to the years with strong SST gradients in the STFZ (2009, 2016, and 2019) (Fig. 2d). Nevertheless, there is no statistically significant correlation between STFZ variability and the SAM index from 1993 to 2021 ($p = 0.11$). In addition, there are some years when a positive SAM has been associated with a positive SAT anomaly at the three inland stations (Supplementary Fig. S2a–c). This means that the enhanced STFZ serves to mitigate the cooling of DML associated with a positive SAM by modifying the atmospheric circulation over the southern Indian Ocean. Consequently, a warming in the interior of the DML has been observed in the 21st century. This is consistent with the fact that the positive SAM pattern has been accompanied by anomalous high pressure over the Indian Ocean sector of East Antarctica since the beginning of the 21st century⁹.

Discussion

The results of this study demonstrate that the SST gradients in the STFZ exert a pivotal influence on the warm half-yearly SAT variability in the eastern DML interior region in EAIS. The STFZ has been strengthened by the rapid SST warming at the basin scale of the Indian Ocean during the 21st century. Interestingly, the observed warming of the Indian Ocean is attributed to the heat uptake by the Pacific Ocean during the negative phase of the Interdecadal Pacific Oscillation (IPO)^{49–51}. During the negative IPO phase, as shown in Fig. 5, prolonged La Niña-like conditions strengthen the Pacific trade winds, which in turn strengthens the Indonesian Throughflow^{49,52}. An increase in the Indonesian Throughflow has led to a greater transfer of warm water to the west of the Indian Ocean via the South Equatorial Current, resulting in a rapid warming of SST at the basin scale over the past two decades (Supplementary Fig. S3b)^{50,53,54}. Therefore, the IPO-induced SST warming in the Indian Ocean is thought to be the trigger for the observed East Antarctic warming. However, the warming of the Indian Ocean is not the

only factor in the variability of the STFZ, and there is an alternative process that could be responsible for the strengthening of the STFZ.

The STFZ variability is characterized by a combination of subtropical warming and mid-latitude Indian Ocean cooling. This meridional dipole pattern of SST anomalies is identical to the negative phase of the Indian Ocean Subtropical Dipole⁵⁵. The negative dipole pattern is associated with a weakening or eastward migration of the Mascarene High, which represents a semi-permanent subtropical high in the southern Indian Ocean^{56–58} (Figs. 5, 6a). As the Mascarene High moves eastward, the low pressure anomaly covers the STFZ (Fig. 6b). The decrease in sea level pressure (SLP) in the STFZ results in an intensification of the meridional SST gradient ($R = -0.50$, $p < 0.05$) (Supplementary Fig. S4). This suggests that anomalous surface winds and upwelling associated with the cyclonic anomalies enhance the vertical mixing with the cooler water below, which in turn strengthens the STFZ. Figure 6c shows less westward migration of the Mascarene High and a decreasing trend of the SLP in the STFZ during the period with increasing SST in the subtropical Indian Ocean. This suggests that the negative phase of the Indian Ocean Subtropical Dipole has become dominant. Over the past 30 years, the SST gradient in the STFZ has increased by about 20%, and atmospheric circulation changes associated with Indian Ocean warming have also contributed to this rapid increase of the SST gradient.

The Mascarene High center position is largely influenced by remote forcing such as the El Niño/Southern Oscillation (ENSO) and the Indian Ocean Dipole (IOD)^{59,60}. The fact that the interannual variability of the Mascarene High position exhibits a robust correlation with both Southern Oscillation Index (SOI) ($R = -0.60$; $p < 0.05$) and IOD index ($R = 0.43$; $p < 0.05$) indicates that the eastward migration of the Mascarene High is strongly linked to the occurrence of both El Niño and a positive IOD (Supplementary Fig. S5)^{56,61,62}. This is in the opposite direction to the above explanation of the Mascarene High moving eastwards during the negative IPO phase. The eastward shift of the Mascarene High from the late 1990s is not an atmospheric response to the ENSO and IOD, but may reflect changes in atmospheric circulation due to the warming of the Indian Ocean. This is supported by the fact that the amplitude of the Mascarene High variability has decreased as the Indian Ocean has warmed (Fig. 6c).

The IPO-induced SST warming over the southern Indian Ocean is a climate variability on a multi-decadal scale. This highlights the importance of natural climate variability in the observed warming trends in the interior of the DML. However, it would not be reasonable to conclude that the robust warming trend in the interior of the DML since the 1990s is attributed solely to natural decadal climate variability. A rapid warming of SST over the Indian Ocean is attributed to increased heat uptake from the atmosphere during the global warming hiatus (2003–2012)^{49–52}. In other words, anthropogenic excess heat is the primary contributor to EAIS warming. Given that the oceans continue to absorb excess heat generated by human activities, it can be said that anthropogenic factors are altering the climate of the East Antarctic interior and making it more vulnerable to atmospheric and oceanic changes.

The impact of Indian Ocean warming on climate change in the interior of Antarctica is not yet fully understood, and thus EAIS warming is a sign that the EAIS is changing rapidly beyond our expectations. The spatial footprint of RLS temperature changes (Supplementary Fig. S1) shows that the rapid warming may be observed over the broad East Antarctic, but no clear warming trends were detected at coastal stations (Fig. 1). This is because local forcing, such as orographic blocking and sea ice variability, may attenuate the warming signal at coastal stations. The warm northerly winds that hit the coast are blocked by the steep topography of the ice sheet and deflected eastwards. They then flow parallel to the coastal slope in a strong current known as a barrier jet^{63–66}. Cold air is entrained from the east and from the katabatic outflow into the barrier jet⁶⁴. This means that the temperature does not rise as much in the coastal region as it

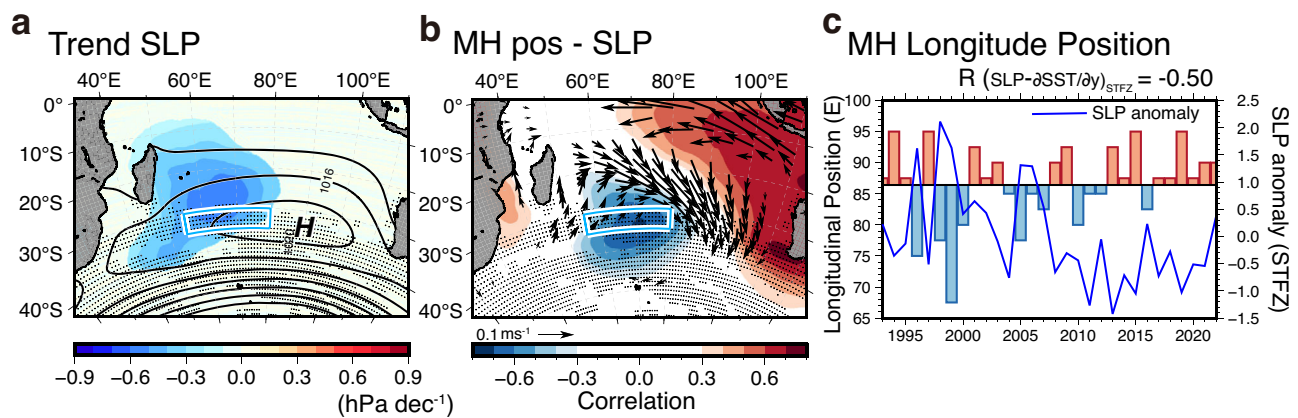


Fig. 6 | Circulation changes over the southern Indian Ocean. a The trend of warm half-year mean sea level pressure (SLP) for 1993–2021. Solid contours represent the SLP climatology for the warm half-year mean. **b** The spatial correlation of the detrended Mascarene High (MH) center position with SLP (shading) and the spatial regression between the detrended MH center position and surface winds (vector) for 1993–2021. **c** The time series of the warm half-year mean MH center position (bar), with the horizontal line indicating the mean for the whole time series

(86.4°E), and SLP anomalies in the subtropical frontal zone (STFZ) region (blue line). The correlation coefficient between SLP anomalies and meridional sea surface temperature (SST) gradients in the STFZ region is shown at the upper right. For all maps, only data points falling within the 90% confidence interval are plotted. The dots indicate the SST frontal zone with SST meridional gradient ($\partial SST/\partial y$) above $0.6\text{ }^{\circ}\text{C } 100\text{ km}^{-1}$. The STFZ region used for comparison with the Relay Station temperature is indicated by the blue box.

does over the ice sheet^{65,67}. Additionally, large sea ice cover along the coast of East Antarctica contributes to reducing the warming signal. Sea ice variability near a station can have a significant impact on the SAT, as sea ice can restrict the heat flux from the relatively warm ocean into the atmosphere. The annual mean SAT at stations on the Antarctic Peninsula is largely affected by the variability of sea ice extent near the stations¹. In contrast, East Antarctic coastal stations experience much smaller annual variations in surface temperature than those on the Antarctic Peninsula as sea ice cover extends far to the north from the coast¹. However, because Antarctic sea ice has decreased significantly and rapidly since 2016, reaching a record minimum in 2023⁶⁸, temperatures at East Antarctic coastal stations may now be more sensitive to sea ice variability than before. Changes in the extent of sea ice are associated with atmospheric circulation, with the occurrence of strong winds resulting in its displacement from or towards the coast. Thus, it can be said that temperatures at coastal stations are susceptible to the influence of Indian Ocean warming. To date, although basal melting of coastal ice is a major contributor of ice loss⁶⁹, warming coastal regions could increase surface melt, leading to additional contributions to sea level rise. Careful monitoring of temperatures not only inland but also in the coastal regions is needed to accurately assess the impact of Indian Ocean warming on climate change in East Antarctica. Research is also needed to confirm the causality of the summer warming using climate model simulations and to explore potential future changes.

Methods

Data

Monthly-mean surface air temperature (SAT) data for the inland Dronning Maud Land (DML) were compiled from the historical AWS observations at Mizuho (MIZ, 70.72°S, 44.26°E, 2180 m a.s.l.), Relay Station (RLS, 74.01°S, 42.98°E, 3354 m a.s.l.), and Dome Fuji (FUJ, 77.33°S, 39.67°E, 3820 m a.s.l.). Multiple AWSs have been installed at these stations since the early 1990s, and observations have been continued to the present day. However, there are several concerns that need to be addressed prior to the integration of multiple AWS data sets into a climate change time series. The major concern is that AWS temperature measurements may have been biased warm in austral summer due to insufficient ventilation in the radiation shield⁷⁰. In this study, these warm biases are quantified by comparison with temperature measurements with an aspirated shield and subsequently removed using a regression model. The other concerns resulting from

changes in the sensor height due to accumulating snow and errors in the early days of the AWS system were also identified by comparing them to other temperature measurements and then removing them. The full description of these corrections is in our previous study¹⁹. After the corrections, multiple AWS records were integrated to create a time series for each station from 1993 to 2022, following the data processing steps used for the Scientific Committee on Antarctic Research (SCAR) Reference Antarctic Data for Environmental Research (READER) database¹⁶. The READER monthly temperature was calculated only if more than 90% of the 6-hourly data was available. To maximize the amount of available data, however, the cutoff percentage for computing the monthly-mean was reduced from 90% to 70% in this study. Comparison of the monthly-mean temperature calculated by randomly selecting 70% of the data with the data using a 90% cutoff percentage shows that the annual mean root mean square error (RMSE) is approximately $0.6\text{ }^{\circ}\text{C}$. This level of error is nearly one-third of the standard deviation of the monthly temperatures¹⁹. The percentage of time between 1993 and 2022 with available monthly-mean SAT data is 72% for FUJ, 79% for RLS, and 51% for MIZ. The detail of AWS observations and the quality-control (QC) procedure are presented in previous research¹⁹. The other monthly-mean SAT data for coastal (Syowa, Mawson) and inland (Amundsen-Scott, Vostok) stations were obtained from the SCAR READER database.

To investigate the atmospheric circulation for 1993–2022, we use monthly-mean fields from ERA5, the fifth generation global atmospheric reanalysis produced by the European Center for Medium-Range Weather Forecasts (ECMWF), which has a spatial resolution of 0.25° and 37 vertical pressure level from 1000 to 10 hPa²⁰. Sea surface temperature (SST) variability over the southern Indian Ocean is studied using the National Oceanic and Atmospheric Administration (NOAA) Optimum interpolated (OI) SST data set, version 2 on 0.25° grid^{71,72}. Changes in storm activity over the southern Indian Ocean are investigated using monthly-mean outgoing longwave radiation (OLR) data obtained from NOAA National Centers for Environmental Information, which has a spatial resolution of 2.5° .

Indices of climate variability modes were used to assess the influence of the observed warming in the interior of East Antarctica. For the SAM index, we used Antarctic Oscillation (AAO) index defined as the leading principal component of 850 hPa geopotential height anomalies south of 20°S ⁷³. The influence of El Niño/ Southern Oscillation (ENSO) was evaluated using the Southern Oscillation index

(SOI), which is a standardized index based on the observed sea level pressure (SLP) difference between Tahiti and Darwin, Australia. We also used the Dipole Mode Index (DMI) for the Indian Ocean Dipole (IOD) intensity⁵⁹.

Reconstruction of the missing SAT

The automatic weather station (AWS) observations are not continuous records, and there are some months with no observations from 1993 to 2022. To fill in the missing records, a reanalysis product was sought which would capture the month-to-month variability of observed temperatures and would not incorporate AWS data into the data assimilation process. A comparison between the monthly mean 2 m temperature (T_{2m}) in the four reanalyses and the observations is shown in Supplementary Fig. S6. Except for JRA-55, all reanalyses show good correspondence to the observations, though lower temperatures (< -40 °C) are overestimated by them. MERRA2 shows optimal performance in simulating the T_{2m} with a root-mean-square error (RMSE) of 2.58 at Dome Fuji (FUJ) and 1.72 at Relay Station (RLS) (Supplementary Fig. S6b, f). ERA5 data agree well with temperature in austral summer, but the discrepancies between ERA5 and observations increase as temperatures decrease (Supplementary Fig. S6a, e). The temperature differences in the austral winter reach up to 5 °C, which results in a relatively larger RMSE for the ERA5 data. Comparable results were reported in a previous study⁷⁴. Although RMSE of MERRA2 is smaller than that of ERA5, there is a concern that MERRA2 T_{2m} at the three stations in inland DML may be affected by the AWS observations through its data assimilation system (See Supplementary Methods). This means that the MERRA2 bias computed by comparison with the AWS observations would underestimate the true model bias in the absence of observations. In contrast, the problem of circularity between the predictor and the predicted variable is avoided for ERA5 due to the fact that the AWS observations do not impact ERA5 T_{2m} (Supplementary Methods). Therefore, ERA5 T_{2m} data were used to fill in the missing observations to create a continuous SAT record for three stations from 1993 to 2022.

ERA5 has an overestimation of lower temperatures (< -40 °C), but otherwise good agreement with observations (Supplementary Fig. S6). To eliminate the inherent bias in ERA5 T_{2m} estimates, a regression model was employed, as the biases show a linear increase with decreasing temperature. It is noteworthy that more than half of AWS data from 1993 to 2009 are independent from the data assimilation system because the data is not available online. The regression model was calibrated using data from 1993 to 2009 (calibrated period) and then tested using data from 2010 to 2022 (tested period) (Supplementary Fig. S10). The RMSE of bias-corrected ERA5 T_{2m} is less than half that of the original ERA5 T_{2m} (Supplementary Figs. S8 and S10). The largest RMSE (1.45 °C) at FUJ, the coldest site, is much lower than that for the other reanalyses (Supplementary Fig. S6). It is worth noting that the RMSE for the tested period is substantially smaller than that for the calibrated period except for MIZ (Supplementary Fig. S10). This implies that the quality of bias-corrected ERA5 T_{2m} is relatively homogeneous over the whole period of the observations.

Uncertainties of reconstructed temperature records

The uncertainties of the bias-corrected ERA5 T_{2m} are assessed through the direct comparison against AWS observations for the 1993–2022 period. The correlation, RMSE, and the bias between monthly observations and ERA5 T_{2m} data are computed at each station. The RMSE of monthly-mean bias-corrected ERA5 T_{2m} is much smaller than the standard deviations of monthly temperatures and is also less than the uncertainty of the AWS observation (1.5 °C) (Supplementary Fig. S11). In addition, the biases of the data with respect to the observations do not depend on the AWS temperature and vary around zero. These suggest that the reliability of monthly mean corrected ERA5 T_{2m} is sufficient to explore the interannual variability of monthly

temperatures during 1993–2022. This is consistent with the smaller RMSE (> 0.9 °C) for the mean seasonal temperatures.

To assess the influence of the infilling of the missing observations with bias-corrected ERA5 on the long-term trend, we compared the time series of the warm and cold half-year mean SAT anomalies at Relay Station, computed from AWS observations and bias-corrected ERA5 (Supplementary Fig. S12). We only focused on Relay Station because of fewer missing values. The half-year mean SAT anomalies were computed from monthly-mean AWS observations only if they were available for more than five months. For comparison, the results of the bias-corrected MERRA2 are also shown in Supplementary Fig. S12. The year-to-year variability of ERA5 captures well the observed variability and amplitude of AWS observations. In particular, the cold half-year mean ERA5 anomalies are in very good agreement with the observations (RMSE=0.18 °C). Despite a slight cold bias in the first half of the observation period (1993–2007), the warm half-year mean of ERA5 is also in good agreement in the second half of the observation period (2008–2021 for warm half-year mean; 2008–2022 for cold half-year mean). The RMSE of ERA5 (0.24 °C) is much smaller than the measurement error (0.40 °C for half-year mean). Thus, we can say that the infilling of the missing observations with bias-corrected ERA5 does not contribute to the warming trend reported in this study. It is noteworthy that the usage of bias-corrected MERRA2 does not reach the same conclusion. The peak-to-peak variability of MERRA2 overestimates the observations. In addition, there is an artificial long-term bias in the MERRA2 time series. In the first half of the observation period (1993–2007), MERRA2 data are warmer than the observations. In contrast, most MERRA2 data are colder than the observations in the second half of the observation period (2008–2021 for warm half-yearly mean; 2008–2022 for cold half-yearly mean). Thus, the warming trend could be underestimated by the infilling of missing observations with MERRA2. This is the main reason for using ERA5 for missing observations.

Statistical methods

Standard least squares linear regression is employed to calculate both trends and regression analysis. A non-parametric Mann-Kendall's test is utilized to assess the annual, semi-annual, and seasonal trends of surface air temperature. Statistical significance is indicated by $p < 0.05$. The two-tailed Student's t-test is used to determine the statistical significance of correlation and regression analysis. The t-score, calculated as the regression model estimate divided by the standard error, was compared to the critical value from the Student's t-distribution with $n-2$ degrees of freedom and the specified confidence level (P).

Data availability

All data used in this study are publicly available. The SAT records from the AWS at Dome Fuji, Relay Station, and Mizuho are available from the Science Database of the National Institute of Polar Research (<https://doi.org/10.17592/002.2025010413>). The complete 30-year SAT data and the bias-corrected ERA5 T_{2m} data at three stations are available from the Antarctic Meteorological Research and Data Center (AMRDC) data repository (<https://doi.org/10.48567/wxxd-7m42>). All other SAT records in this study are obtained from the Scientific Committee on Antarctic Research (SCAR) Reference Antarctic Data for Environmental Research (READER) database (<https://www.bas.ac.uk/project/reader/#data>). ERA5 data are available online at <https://cds.climate.copernicus.eu/datasets>. NOAA OI SST v2 data are available online at <http://www.esrl.noaa.gov/psd/data/gridded/data.noaa.oisst.v2.html>. OLR data are available online from NOAA National Centers for Environmental Information at <https://doi.org/10.7289/V5W37TKD>. The climate indices are available online at the following website: AAO from <https://stateoftheocean.osmc.noaa.gov/atm/sam.php>, SOI from <https://www.cpc.ncep.noaa.gov/data/indices/soiand> IOD https://ds.data.jma.go.jp/tcc/tcc/products/el_nino/index/iod_index.html.

Code availability

All code used to produce the results and figures of this paper is available from the first author upon request. All of the custom code is based on published implementations of standard methods and statistical techniques. Ruby and python3 are used for data processing and analysis. All figures were plotted with Generic Mapping Tools (GMT) (<https://www.generic-mapping-tools.org>) and further modified with Adobe Illustrator (<https://www.adobe.com/products/illustrator.html>).

References

1. Turner, J. et al. Antarctic temperature variability and change from station data. *Int. J. Climatol.* **40**, 2986–3007 (2020).
2. Thompson, D. W. J. & Solomon, S. Interpretation of recent southern hemisphere climate change. *Science* **296**, 895–899 (2002).
3. Marshall, G. J. Half-century seasonal relationships between the southern annular mode and Antarctic temperatures. *Int. J. Climatol.* **27**, 373–383 (2007).
4. Nicolas, J. P. & Bromwich, D. H. New reconstruction of Antarctic near-surface temperatures: Multidecadal trends and reliability of global reanalyses. *J. Clim.* **27**, 8070–8093 (2014).
5. Marshall, G. J. & Thompson, D. W. J. The signatures of large-scale patterns of atmospheric variability in antarctic surface temperatures. *J. Geophys. Res. Atmos.* **121**, 3276–3289 (2016).
6. Fogt, R. L. & Marshall, G. J. The southern annular mode: Variability, trends, and climate impacts across the Southern Hemisphere. *WIREs Clim. Change* **11**, e652 (2020).
7. Jones, M. E. et al. Sixty years of widespread warming in the southern mid- and high-latitudes (1957–2016). *J. Clim.* **32**, 6875–6898 (2019).
8. Stokes, C. R. et al. Response of the East Antarctic ice sheet to past and future climate change. *Nature* **608**, 275–286 (2022).
9. Marshall, G. J., Orr, A. & Turner, J. A predominant reversal in the relationship between the SAM and East Antarctic temperatures during the twenty-first century. *J. Clim.* **26**, 5196–5204 (2013).
10. Clem, K. R., Lintner, B. R., Broccoli, A. J. & Miller, J. R. Role of the South Pacific convergence zone in West Antarctic decadal climate variability. *Geophys. Res. Lett.* **46**, 6900–6909 (2019).
11. Clem, K. R. et al. Record warming at the South Pole during the past three decades. *Nature Clim. Change* **10**, 762–770 (2020).
12. Xin, M. et al. A broadscale shift in antarctic temperature trends. *Clim. Dynam.* **61**, 4623–4641 (2023).
13. Wachter, P., Beck, C., Philipp, A., Höppner, K. & Jacobeit, J. Spatiotemporal variability of the southern annular mode and its influence on Antarctic surface temperatures. *J. Geophys. Res. Atmos.* **125**, e2020JD033818 (2020).
14. Campitelli, E., Diaz, L. B. & Vera, C. Assessment of zonally symmetric and asymmetric components of the southern annular mode using a novel approach. *Clim. Dynam.* **58**, 161–178 (2022).
15. Boschat, G., Purich, A., Rudeva, I. & Arblaster, J. Impact of zonal and meridional atmospheric flow on surface climate and extremes in the Southern Hemisphere. *J. Clim.* **36**, 5041–5061 (2023).
16. Turner, J. et al. The SCAR READER project: Toward a high-quality database of mean Antarctic meteorological observations. *J. Clim.* **17**, 2890–2898 (2004).
17. Retamales-Muñoz, G., Durán-Alarcón, C. & Mattar, C. Recent land surface temperature patterns in antarctica using satellite and reanalysis data. *J. South Am. Earth Sci.* **95**, 102304 (2019).
18. Zhang, X., Wang, Y., Hou, S. & Heil, P. Significant West Antarctic cooling in the past two decades driven by tropical Pacific forcing. *BAMS*. **104**, E1154–E1165 (2023).
19. Kurita, N. et al. Near-surface air temperature records over the past 30 years in the interior of Dronning Maud Land, East Antarctica. *J. Atmos. and Ocean. Tech.* **41**, 179–188 (2024).
20. Hersbach, H. et al. The ERA5 global reanalysis. *Quart. J. Roy. Meteor. Soc.* **146**, 1999–2049 (2020).
21. Nicolas, J. P. & Bromwich, D. H. Climate of West Antarctica and influence of marine air intrusions. *J. Clim.* **24**, 49–67 (2011).
22. Bromwich, D. H. et al. Central West Antarctica among the most rapidly warming regions on earth. *Nat. Geosci.* **6**, 1–7 (2012).
23. Nicolas, J. P. et al. January 2016 extensive summer melt in West Antarctica favoured by strong El Niño. *Nat. Commun.* **8**, 15799 (2017).
24. Wille, J. D. et al. West antarctic surface melt triggered by atmospheric rivers. *Nat. Geosci.* **12**, 911–916 (2019).
25. Wille, J. D. et al. The extraordinary March 2022 East Antarctica “Heat” Wave. part i: Observations and meteorological drivers. *J. Clim.* **37**, 757–778 (2024).
26. Ding, Q., Steig, E. J., Battisti, D. S. & Küttel, M. Winter warming in West Antarctica caused by central tropical Pacific warming. *Nat. Geosci.* **6**, 398–403 (2011).
27. Schneider, D. P., Okumura, Y. & Deser, C. Observed Antarctic interannual climate variability and tropical linkages. *J. Clim.* **25**, 4048–4066 (2012).
28. Turner, J. et al. Absence of 21st century warming on Antarctic Peninsula consistent with natural variability. *Nature*. **7612**, 411–415 (2016).
29. Clem, K. R., Orr, A. & Pope, J. O. The springtime influence of natural tropical Pacific variability on the surface climate of the Ross ice shelf, West Antarctica: Implications for ice shelf thinning. *Sci. Rep.* **8**, 11983 (2018).
30. Yiu, Y. Y. S. & Maycock, A. C. On the seasonality of the El Niño teleconnection to the Amundsen sea region. *J. Clim.* **32**, 4829–4845 (2019).
31. Raphael, M. N. The influence of atmospheric zonal wave three on Antarctic sea ice variability. *J. Geophys. Res. Atmos.* **112**, D12112 (2007).
32. Goyal, R., Jucker, M., Gupta, A. S. & England, M. H. A new zonal wave-3 index for the Southern Hemisphere. *J. Clim.* **35**, 5137–5149 (2022).
33. Raphael, M. N. A zonal wave 3 index for the Southern Hemisphere. *Geophys. Res. Lett.* **31**, L23212 (2004).
34. Fogt, R. L., Jones, J. M. & Renwick, J. Seasonal zonal asymmetries in the Southern Annular Mode and their impact on regional temperature anomalies. *J. Clim.* **25**, 6253–6270 (2012).
35. Senapati, B., Deb, P., Dash, M. K. & Behera, S. K. Origin and dynamics of global atmospheric wavenumber-4 in the southern mid-latitude during austral summer. *Clim. Dyn.* **59**, 1309–1322 (2022).
36. Graham, R. M. & Boer, A. M. D. The dynamical subtropical front. *J. Geophys. Res. Ocean* **118**, 5676–5685 (2013).
37. Menezes, V. V. et al. South Indian countercurrent and associated fronts. *J. Geophys. Res. Ocean* **119**, 6783–6791 (2014).
38. Kostianoy, A. G., Ginzburg, A. I., Frankignoulle, M. & Delille, B. Fronts in the southern Indian Ocean as inferred from satellite sea surface temperature data. *J. Mar. Syst.* **45**, 55–73 (2004).
39. Nakamura, H., Sampe, T., Tanimoto, Y. & Shimpo, A. Wang, C., Xie, S.-P. & Carton, J. A. (eds) *Observed associations among storm tracks, jet streams and midlatitude oceanic fronts: The ocean-atmosphere interaction*. (eds Wang, C., Xie, S.-P. & Carton, J. A.) *Earth’s Climate: The Ocean-Atmosphere Interaction*, Geophysical Monograph Series, 329–345 (American Geophysical Union, Washington, DC, 2004).
40. Nakamura, H., Sampe, T., Goto, A., Ohfuchi, W. & Xie, S.-P. On the importance of midlatitude oceanic frontal zones for the mean state and dominant variability in the tropospheric circulation. *Geophys. Res. Lett.* **35**, L15709 (2008).
41. Sampe, T., Nakamura, H., Goto, A. & Ohfuchi, W. Significance of a midlatitude SST frontal zone in the formation of a storm track and an eddy-driven westerly jet. *J. Clim.* **23**, 1793–1814 (2010).
42. Rao, Q.-R., Zhang, L., Ren, X. & Wu, L. Atmospheric responses to the interannual variability of sea surface temperature front in the summertime Southern Ocean. *Clim. Dynam.* **62**, 3689–3707 (2024).

43. Fang, J. & Yang, X.-Q. Structure and dynamics of decadal anomalies in the wintertime midlatitude North Pacific ocean-atmosphere system. *Clim. Dynam.* **47**, 1989–2007 (2016).
44. Wang, L.-Y., Hu, H.-B. & Yang, X.-Q. The atmospheric responses to the intensity variability of subtropical front in the wintertime North Pacific. *Clim. Dynam.* **52**, 5623–5639 (2019).
45. Tao, L., Sun, X. & Yang, X.-Q. The asymmetric atmospheric response to the midlatitude North Pacific SST anomalies. *J. Geophys. Res. Atmos.* **124**, 9222–9240 (2019).
46. Chen, Q., Hu, H., Ren, X. & Yang, X.-Q. Numerical simulation of midlatitude upper-level zonal wind response to the change of North Pacific subtropical front strength. *J. Geophys. Res. Atmos.* **124**, 4891–4912 (2019).
47. Kushnir, Y. et al. Atmospheric GCM response to extratropical SST anomalies: Synthesis and evaluation. *J. Clim.* **15**, 2233–2256 (2002).
48. Small, R. J., Tomas, R. A. & Bryan, F. O. Storm track response to ocean fronts in a global high-resolution climate model. *Clim. Dynam.* **43**, 805–828 (2014).
49. Lee, S.-K. et al. Pacific origin of the abrupt increase in Indian Ocean heat content during the warming hiatus. *Nat. Geosci.* **8**, 445–449 (2015).
50. Li, Y., Han, W. & Zhang, L. Enhanced decadal warming of the southeast Indian Ocean during the recent global surface warming slowdown. *Geophys. Res. Lett.* **44**, 9876–9884 (2017).
51. Vidya, P. J., Ravichandran, M., Subeesh, M. P., Chatterjee, S. & Nuncio, M. Global warming hiatus contributed weakening of the Mascarene High in the Southern Indian Ocean. *Sci. Rep.* **10**, 3255 (2020).
52. Dong, L. & McPhaden, M. J. Interhemispheric SST gradient trends in the Indian Ocean prior to and during the recent global warming hiatus. *J. Clim.* **29**, 9077–9095 (2016).
53. Zhang, Y. et al. Strengthened Indonesian throughflow drives decadal warming in the Southern Indian Ocean. *Geophys. Res. Lett.* **45**, 6167–6175 (2018).
54. Jyoti, J., Swapna, P., Krishnan, R. & Naidu, C. V. Pacific modulation of accelerated south Indian Ocean sea level rise during the early 21st century. *Clim. Dynam.* **53**, 4413–4432 (2019).
55. Behera, S. K. & Yamagata, T. Subtropical SST dipole events in the southern Indian Ocean. *Geophys. Res. Lett.* **28**, 327–330 (2001).
56. Manatsa, D., Morioka, Y., Behera, S. K., Matarira, C. H. & Yamagata, T. Impact of Mascarene High variability on the East African ‘short rains’. *Clim. Dynam.* **42**, 1259–1274 (2014).
57. Ohishi, S., Sugimoto, S. & Hanawa, K. Zonal movement of the Mascarene high in austral summer. *Clim. Dynam.* **45**, 1739–1745 (2015).
58. Morioka, Y., Takaya, K., Behera, S. K. & Masumoto, Y. Local SST impacts on the summertime Mascarene High variability. *J. Clim.* **28**, 678–694 (2015).
59. Saji, N. H., Goswami, B. N., Vinayachandran, P. N. & Yamagata, T. A dipole mode in the tropical Indian ocean. *Nature*. **401**, 360–363 (1999).
60. Morioka, Y., Takaya, K., Behera, S. K. & Masumoto, Y. Role of tropical SST variability on the formation of subtropical dipoles. *J. Clim.* **27**, 4486–4507 (2014).
61. Morioka, Y., Tozuka, T. & Yamagata, T. How is the Indian Ocean subtropical dipole excited? *Clim. Dynam.* **41**, 1955–1968 (2013).
62. Xulu, N. G., Chikoore, H., Bopape, M.-J. M. & Nethengwe, N. S. Climatology of the Mascarene High and its influence on weather and climate over Southern Africa. *Climate* **8**, 86 (2020).
63. Bromwich, D. H. Snowfall in high southern latitudes. *Rev. of Geophys.* **26**, 149–168 (1988).
64. Bromwich, D. H., Steinhoff, D. F., Simmonds, I., Keay, K. & Fogt, R. L. Climatological aspects of cyclogenesis near Adélie Land Antarctica. *Tellus A.* **63**, 921–938 (2011).
65. Yamada, K. & Hirasawa, N. Analysis of a record-breaking strong wind event at Syowa station in January 2015. *J. Geophys. Res. Atmos.* **123**, 13643–13657 (2018).
66. Gorodetskaya, I. V., Silva, T., Schmithüsen, H. & Hirasawa, N. Atmospheric river signatures in radiosonde profiles and reanalyses at the Dronning Maud Land coast, East Antarctica. *Adv. Atmos. Sci.* **37**, 455–476 (2020).
67. Turner, J. et al. An extreme high temperature event in coastal East Antarctica associated with an atmospheric river and record summer downslope winds. *Geophys. Res. Lett.* **49**, e2021GL097108 (2022).
68. Purich, A. & Doddridge, E. W. Record low Antarctic sea ice coverage indicates a new sea ice state. *Nat. Commun.* **4**, 314 (2023).
69. Rignot, E. et al. Ice-shelf melting around Antarctica. *Science* **341**, 266–270 (2013).
70. Morino, S. et al. Comparison of ventilated and unventilated air temperature measurements in inland Dronning Maud Land on the East Antarctic Plateau. *J. Atmos. Oceanic Technol.* **38**, 2061–2070 (2021).
71. Reynolds, R. W. et al. Daily high-resolution-blended analyses for sea surface temperature. *J. Clim.* **20**, 5473–5496 (2007).
72. Huang, B. et al. Improvements of the daily optimum interpolation sea surface temperature (DOISST) version 2.1. *J. Clim.* **34**, 2923–2939 (2021).
73. Thompson, D. W. & Wallace, J. M. Annular modes in the extratropical circulation. part i: month-to-month variability. *J. Clim.* **13**, 1000–1016 (2000).
74. Gossart, A. et al. An evaluation of surface climatology in state-of-the-art reanalyses over the Antarctic ice sheet. *J. Clim.* **32**, 6899–6915 (2019).

Acknowledgements

We acknowledge the Japan Antarctic Research Expedition (JARE), which is responsible for the AWS observations in Antarctica. The authors also thank the US National Science Foundation for its support of the AWS network, grant #2301362 and analysis support from grant #2205398. This paper is dedicated to the memory of Hiroyuki Yamada, who passed away in October 2024.

Author contributions

N.K. conceived the study, created the continuous SAT data set, analyzed all of the results, led the writing of the manuscript and prepared all figures. D.H.B., D.E.M., L.M.K., N.H. and M.A.L. contributed to discussions of analysis design and to writing and revising the manuscript. N.K., T.K., H.M., N.H., D.E.M., L.M.K., M.A.L. contributed to obtaining SAT data from AWS observations. All co-authors refined the manuscript content.

Competing interests

The authors declare no competing interests.

Additional information

Supplementary information The online version contains supplementary material available at <https://doi.org/10.1038/s41467-025-61919-3>.

Correspondence and requests for materials should be addressed to Naoyuki Kurita.

Peer review information *Nature Communications* thanks the anonymous reviewers for their contribution to the peer review of this work. A peer review file is available.

Reprints and permissions information is available at <http://www.nature.com/reprints>

Publisher's note Springer Nature remains neutral with regard to jurisdictional claims in published maps and institutional affiliations.

Open Access This article is licensed under a Creative Commons Attribution-NonCommercial-NoDerivatives 4.0 International License, which permits any non-commercial use, sharing, distribution and reproduction in any medium or format, as long as you give appropriate credit to the original author(s) and the source, provide a link to the Creative Commons licence, and indicate if you modified the licensed material. You do not have permission under this licence to share adapted material derived from this article or parts of it. The images or other third party material in this article are included in the article's Creative Commons licence, unless indicated otherwise in a credit line to the material. If material is not included in the article's Creative Commons licence and your intended use is not permitted by statutory regulation or exceeds the permitted use, you will need to obtain permission directly from the copyright holder. To view a copy of this licence, visit <http://creativecommons.org/licenses/by-nc-nd/4.0/>.

© The Author(s) 2025